Received: 9 April 2019 | Revised: 9 August 2019 | Accepted: 3 September 2019

DOI: 10.1002/hbm.24795

RESEARCH ARTICLE

WILEY

Potential of on-scalp MEG: Robust detection of human visual gamma-band responses

Joonas Iivanainen[1] | Rasmus Zetter[1] | Lauri Parkkonen[1,2]

[1]Department of Neuroscience and Biomedical Engineering, Aalto University School of Science, Espoo, Finland

[2]Aalto Neuroimaging, Aalto University, Espoo, Finland

Correspondence
Joonas Iivanainen and Rasmus Zetter, Department of Neuroscience and Biomedical Engineering, Aalto University School of Science, FI-00076 Aalto, Finland.
Email: joonas.iivanainen@aalto.fi (J. I.);
Email: rasmus.zetter@aalto.fi (R. Z.)

Funding information
H2020 European Research Council, Grant/Award Number: 678578; Instrumentarium Science Foundation, Grant/Award Number: 180043; National Institute of Neurological Disorders and Stroke, Grant/Award Number: R01NS094604; Finnish Cultural Foundation, Grant/Award Numbers: 00170330, 00180388

Abstract

Electrophysiological signals recorded intracranially show rich frequency content spanning from near-DC to hundreds of hertz. Noninvasive electromagnetic signals measured with electroencephalography (EEG) or magnetoencephalography (MEG) typically contain less signal power in high frequencies than invasive recordings. Particularly, noninvasive detection of gamma-band activity (>30 Hz) is challenging since coherently active source areas are small at such frequencies and the available imaging methods have limited spatial resolution. Compared to EEG and conventional SQUID-based MEG, on-scalp MEG should provide substantially improved spatial resolution, making it an attractive method for detecting gamma-band activity. Using an on-scalp array comprised of eight optically pumped magnetometers (OPMs) and a conventional whole-head SQUID array, we measured responses to a dynamic visual stimulus known to elicit strong gamma-band responses. OPMs had substantially higher signal power than SQUIDs, and had a slightly larger relative gamma-power increase over the baseline. With only eight OPMs, we could obtain gamma-activity source estimates comparable to those of SQUIDs at the group level. Our results show the feasibility of OPMs to measure gamma-band activity. To further facilitate the noninvasive detection of gamma-band activity, the on-scalp OPM arrays should be optimized with respect to sensor noise, the number of sensors and intersensor spacing.

KEYWORDS
gamma band, magnetoencephalography, optically pumped magnetometer, visual system

1 | INTRODUCTION

Neuronal gamma-band (>30 Hz) synchronization appears to be a fundamental part of neural communication in the brain, having been linked to a multitude of cognitive functions, such as attentional selection (Fries, Reynolds, Rorie, & Desimone, 2001; Tallon-Baudry, Bertrand, Delpuech, & Pernier, 1996) and working memory (Howard et al., 2003; Pesaran, Pezaris, Sahani, Mitra, & Andersen, 2002). The interest in electrophysiological gamma-band signals (the "gamma buzz"; Buzsaki, 2006; Lachaux, Axmacher, Mormann, Halgren, & Crone, 2012) was initiated by studies in the cat visual cortex that suggested that the binding of visual stimulus features might be mediated by neuronal synchronization at frequencies around 40 Hz (Eckhorn et al., 1988; Gray, König, Engel, & Singer, 1989); the idea was then formulated as the binding-by-synchrony hypothesis (Singer, 1999). More recently, it has been also hypothesized that the precise timing of the gamma oscillations plays a key role in information transfer between different cortical regions (Fries, 2015). While these hypotheses have assumed an

Joonas Iivanainen and Rasmus Zetter contributed equally to this study.

oscillatory mechanism (usually present as a signal increase in a narrow frequency band; narrowband gamma), it is now appreciated that stimulation also usually induces a broadband (40–150 Hz) increase in signal power (broadband gamma or high-frequency activity; Crone, Korzeniewska, & Franaszczuk, 2011, Lachaux et al., 2012). Broadband gamma has been shown to be correlated with multiunit activity, reflecting local cortical processing (Manning, Jacobs, Fried, & Kahana, 2009; Ray, Crone, Niebur, Franaszczuk, & Hsiao, 2008; Ray & Maunsell, 2011).

Evidence of the link between gamma-band activity and cognitive functions was originally discovered in invasive experiments in non-human animals (e.g., Eckhorn et al., 1988; Fries et al., 2001; Gray et al., 1989). Similar findings were then reported in invasive human measurements using intracranial electroencephalography (iEEG) (e.g., Crone, 1998; Crone, Boatman, Gordon, & Hao, 2001). Gamma-band activity has also been observed noninvasively in humans using scalp-EEG (e.g., Ball et al., 2008; Pfurtscheller & Neuper, 1992; Tallon-Baudry et al., 1996) and magnetoencephalography (MEG) (e.g., Adjamian et al., 2004; Hoogenboom, Schoffelen, Oostenveld, Parkes, & Fries, 2006). However, it is commonly understood that the noninvasive detection of gamma-band activity is difficult due to poor signal-to-noise ratio (SNR) and spatial resolution of the measurement methods (e.g., Dalal et al., 2009; Jerbi et al., 2009). Thus, the studies have usually relied on special stimuli crafted to maximize the gamma SNR.

The disparity in the SNR between invasively and noninvasively measured neural activity is dependent on the frequency: lower-frequency activity such as alpha (∼10 Hz) and beta (∼20 Hz) rhythms are typically equally present in noninvasive and invasive measurements, while higher frequency activity is proportionally much weaker in noninvasive measurements (Jerbi et al., 2009). A likely reason for the low SNR of gamma-band signals detected by EEG/MEG is the short coherence length of the gamma sources, that is, a patch of cortex producing synchronous gamma activity is smaller than a patch producing synchronous activity at lower frequencies (for experimental evidence in somatomotor cortex see, e.g., Pfurtscheller, Graimann, Huggins, Levine, & Schuh, 2003 and Miller et al., 2007).

The spatial resolution of EEG is inherently limited by the spatial low-pass filtering of the neural electric field by the conductivity structure of the head (Srinivasan, Tucker, & Murias, 1998); the filtering leads to loss of spatial detail so that nearby sources cannot be separated easily or at all. By contrast, the neuromagnetic field measured by MEG is not as sensitive to head tissue conductivities (Hämäläinen, Hari, Lounasmaa, Knuutila, & Ilmoniemi, 1993; Iivanainen, Stenroos, & Parkkonen, 2017; Stenroos & Nummenmaa, 2016) so that the spatial detail of the field is mostly determined by the measurement distance. In conventional SQUID-based MEG, the distance of the sensors to the head (at least about 2 cm) thus limits the spatial resolution.

Recent advances in the development of optically pumped magnetometers (OPMs) (Budker & Kimball, 2013; Budker & Romalis, 2007) has enabled their use in MEG (e.g., Borna et al., 2017; Boto et al., 2018; Iivanainen, Zetter, Grön, Hakkarainen, & Parkkonen, 2019; Sheng, Wan, et al., 2017). OPMs, in contrast to SQUIDs, can be placed in very close proximity to the scalp, considerably boosting both spatial resolution and sensitivity to neural sources (Boto et al., 2016; Iivanainen et al., 2017). Thus, OPM-based on-scalp MEG shows great promise both generally in the context of MEG and specifically for the detection of gamma-band activity.

In this work, we demonstrate that visual gamma-band responses can reliably be detected with on-scalp MEG based on currently available OPMs at a similar or better SNR than with conventional SQUID-based MEG. Additionally, we demonstrate that source-level analysis of gamma activity can be performed with a limited number of channels only covering parts of the scalp.

2 | MATERIALS AND METHODS

2.1 | Subjects

Ten healthy volunteers (six males, four females, 23–33 years of age, average 27.7 years) with no known history of neurological or psychiatric disorders participated in the study. The experimental design took into consideration the code of ethics as defined in the World Medical Association's Declaration of Helsinki, and the study was approved by the Aalto University Ethics Committee. Informed consent was obtained from all participants.

2.2 | Structural MRI acquisition and segmentation

T1-weighted structural MR images from previous studies were available for all subjects. The FreeSurfer software package (Dale, Fischl, & Sereno, 1999; Fischl, 2012; Fischl, Sereno, Tootell, & Dale, 1999) was used for preprocessing the MRIs and for segmentation of the cortical surfaces. For each subject, the surfaces of the skull and scalp were segmented using the watershed approach (Ségonne et al., 2004) implemented in FreeSurfer and MNE software (Gramfort et al., 2014). These surfaces were thereafter decimated to obtain three boundary element meshes (2,562 vertices per mesh). For source estimation, the neural activity was modeled as a primary current distribution constrained to the surface separating the cortical gray and white matter and discretized into a set current dipoles (4,098 locations per hemisphere, three orthogonal dipoles per location).

2.3 | Experimental paradigm and stimuli

To evoke visual gamma-band activity, we used a stimulation paradigm originally presented by Hoogenboom et al. (2006) and thereafter employed in a multitude of studies (e.g., Hoogenboom, Schoffelen, Oostenveld, & Fries, 2010; Scheeringa et al., 2011; Tan, Gross, & Uhlhaas, 2016; van Pelt, Shumskaya, & Fries, 2018). In short, the experiment consisted of contracting sine-wave gratings projected on a screen in front of the subject inside a magnetically shielded room (MSR). In 80% of the trials, the contraction velocity of the grating increased at an unpredictable time but not earlier than 50 ms after the stimulus onset; the subject's task was to detect this increase and report it as quickly as possible by lifting the right index finger. The remaining 20% of the trials were a catch condition during which no

velocity increase occurred. After each response, visual feedback of the correctness of the subject's response was given.

The parameters of the stimulation paradigm were the same as in the work by Scheeringa et al. (2011). The stimuli were projected on a semi-transparent back-projection screen using a projector (ET-LAD7700/L; Panasonic, Osaka, Japan; lens ET-D75LE3; refresh rate 60 Hz; resolution 1,280 × 1,024), located outside the MSR. The distance from the eyes to the screen and the stimulus size were adjusted such that the outer diameter of the grating subtended a visual angle of 5°. Stimuli were presented using the "Presentation" software package (Neurobehavioral Systems, Inc., Berkeley, CA). Subject responses (finger lifts) were recorded using an in-house-built optically triggered button.

During an approximately 1.5-hr session (including subject preparation), the experiment was performed for each subject using both OPM- and SQUID-MEG. The order of OPM and SQUID measurements was counterbalanced across subjects. Each subject completed one block of 100 trials per measurement, which lasted approximately 12 min. A 1-min resting-state measurement was performed after the primary task was completed.

2.4 | MEG acquisition

OPM-MEG was recorded using an array of eight OPMs (Gen-1.0 QZFM; QuSpin Inc., Louisville, CO). The measurement setup is depicted in Figure 1. The OPMs were placed in a 3D-printed helmet with identical geometry to that of a commercial 306-channel SQUID-MEG system (MEGIN Oy [formerly Elekta Oy], Helsinki, Finland). Individual OPMs were placed into sockets in the helmet, whose positions and orientations corresponded to those of the occipital sensors of the MEGIN system, and inserted until touching the head of the subject. The insertion depth was manually measured for each sensor. The helmet was attached to the chair the subject was seated in, and the subject's head position inside the helmet was adjusted so that the OPM array covered the occipital cortex. To fix the position of the subject's head inside the helmet, dummy sensors were inserted into sockets on the sides of the helmet so that they gently pressed on the head on each side. MEG–MRI coregistration was performed using an optical scanner as described by Zetter, Iivanainen, and Parkkonen (2019); an example of coregistered OPM positions with respect to the subject's head is shown in Figure 1. For Subjects 1 and 2, an additional ninth OPM was used (seen in Figure 1, left side); however, for these subjects, one OPM malfunctioned and was not included in the analysis. The OPM data (sensor bandwidth ∼130 Hz) were recorded at 1-kHz sampling rate with an acquisition passband of 0.03–330 Hz using a data acquisition system based on the electronics of the commercial MEGIN system (Iivanainen et al., 2019). No additional magnetic shielding was used for the OPMs; the ambient-field amplitude and its drift inside our three-layer MSR (Imedco AG, Hägendorf, Switzerland) are typically below ∼10 nT and ∼30 pT/hr, respectively, and thus do not pose any challenges for the operation of the OPMs (Iivanainen et al., 2019).

SQUID-MEG was recorded using a whole-head 306-channel MEG system (Vectorview by MEGIN/Elekta Oy; 102 magnetometers; 204 planar gradiometers). The MEG signal was acquired with the same acquisition parameters as in OPM-MEG. MEG–MRI coregistration was performed using an electromagnetic digitizer in conjunction with head position indicator (HPI) coils. Approximately ∼150 head-shape points were digitized and five HPI coils were applied. In both measurement modalities, 1 min of data in the absence of a subject was also recorded.

2.5 | Data analysis

We performed all MEG analysis using the MNE-Python software (master branch, checked out on October 19, 2018; Gramfort et al., 2014). Both OPM and SQUID data were band-pass filtered to 0.1–130 Hz before further processing. Epochs were manually inspected and those containing visible artifacts were rejected.

FIGURE 1 Left: The optically pumped magnetometer (OPM) measurement setup in the magnetically shielded room (MSR). Right: SQUID (top) and OPM (bottom) sensor positions with respect to the head of a representative subject. The source space used for OPM source estimation is shown as yellow points

2.5.1 | Sensor-level analysis

Time–frequency representations (TFRs) of the responses were computed using Morlet wavelets. The frequency spacing for the TFR computation was 1 Hz, with the number of cycles for each frequency *f* set to *f*2. The 2.5-s period preceding stimulation was used as a baseline.

Power spectral density (PSD) was computed using a multitaper approach. Multiple orthogonal tapers (Slepian, 1978) were applied to each epoch, after which the spectral density of each channel was computed by averaging over each taper and epoch. The bandwidth of the multitaper window function was set to 1 Hz. For baseline spectra, the 2.0–0.5-s period preceding stimulation was used. For the stimulation-period spectra, the time period 0.5–2.0 s following stimulation onset was used; the contribution of the initial evoked responses to the spectra was thus avoided.

For quantitative analysis of the difference in spectral power between stimulation and baseline, we computed the ratio between the stimulation and baseline spectra for each sensor. Thereafter, we fitted a Gaussian function to the gamma-band peak in the relative spectrum of each sensor using the Trust Region Reflective algorithm as implemented in the *scipy* software library (Jones, Oliphant, Peterson, et al., 2001). We estimated the gamma power increase (stimulation vs. baseline) by the peak amplitude of the Gaussian, the gamma frequency by the Gaussian peak frequency and the gamma bandwidth by the full width at half maximum (FWHM) of the Gaussian. The Gaussian function amplitude (i.e., the power increase relative to baseline) was constrained to be higher than 0.1%, peak frequency was bounded to 40–70 Hz and the bandwidth (FWHM) to 3–47 Hz. The fitting was initialized with a guess amplitude of 11, center frequency of 52 Hz, and a bandwidth of 9.4 Hz. In addition, the goodness-of-fits (GOFs) of the Gaussians were computed. Sensors for which the fitted Gaussian function had a GOF less than 0.5 or amplitude less than 5% were considered not to have a gamma response. This relative spectral power analysis was performed for all subjects for both OPM and SQUID data.

2.5.2 | Source-level analysis

Forward models were computed using the MRI-derived three-shell boundary element models (see Section 2.2). OPMs were modeled as by Zetter, Iivanainen, Stenroos, and Parkkonen (2018), with eight integration points equally spaced within a 3-mm cube corresponding to the sensitive volume of the sensor. SQUIDs were modeled as in the MNE software. For the SQUID measurement, the 102 magnetometers and the entire whole-brain source space were used in the analysis. Due to the small number of OPM sensors, we restricted the source space in OPM analysis to cortical locations within 7 cm of the sensors, limiting the number of points in the source space to 2,361 ± 197 (mean ± *SD*) across subjects. The source space for a representative subject is shown in Figure 1. The subject-specific sensitivity maps that were used to determine the 7-cm limit are shown in Figure S1, Supporting Information. For the SQUID measurements, signal-space projection (Uusitalo & Ilmoniemi, 1997) based on an empty-room recording was applied to suppress artifacts in frontal channels that would otherwise corrupt the source estimates.

For source-level estimation of induced power, we employed DICS beamforming (Gross et al., 2001) as implemented in MNE-Python. To speed up computation, data were decimated by a factor of 3 before analysis. Cross-spectral density (CSD) matrices for baseline (2.0–0.5 s preceding stimulus onset) and stimulation (0.5–2.0 s following stimulus onset) time periods were computed within two frequency bands corresponding to alpha and gamma bands. The alpha frequency band (7–13 Hz) was chosen on the basis of sensor-level TFRs to encompass alpha-band activity for all subjects. Subject-specific gamma bands were defined using the peak frequencies and bandwidths given by the Gaussian fits. Since SQUID magnetometer gamma bands were

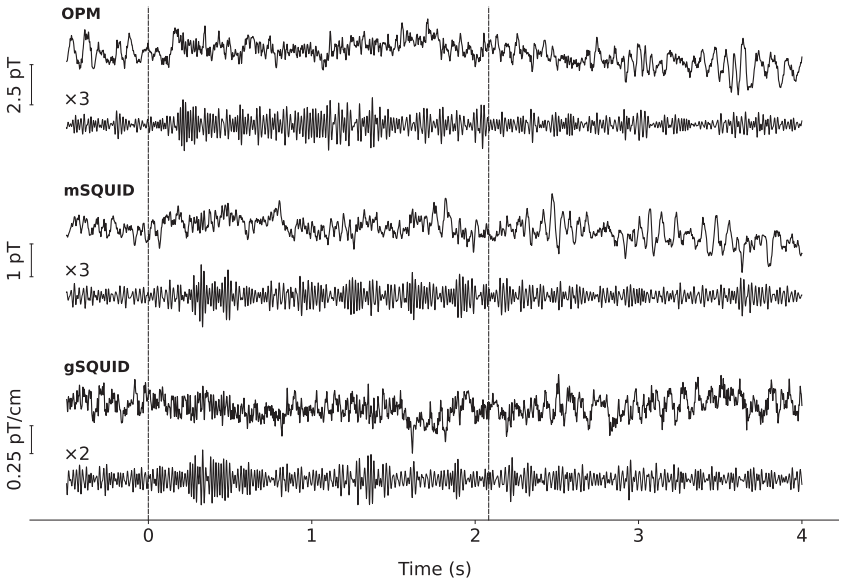

FIGURE 2 A representative single-trial response filtered to 0.1–130 Hz (upper traces) and to 40–70 Hz (lower traces) of optically pumped magnetometer (OPM), SQUID magnetometer (mSQUID), and planar SQUID gradiometer (gSQUID) sensor with the largest gamma-band response (Subject 6). The dashed vertical lines indicate the onset and offset of the stimulus. Responses are from a trial without a change in the grating contraction velocity

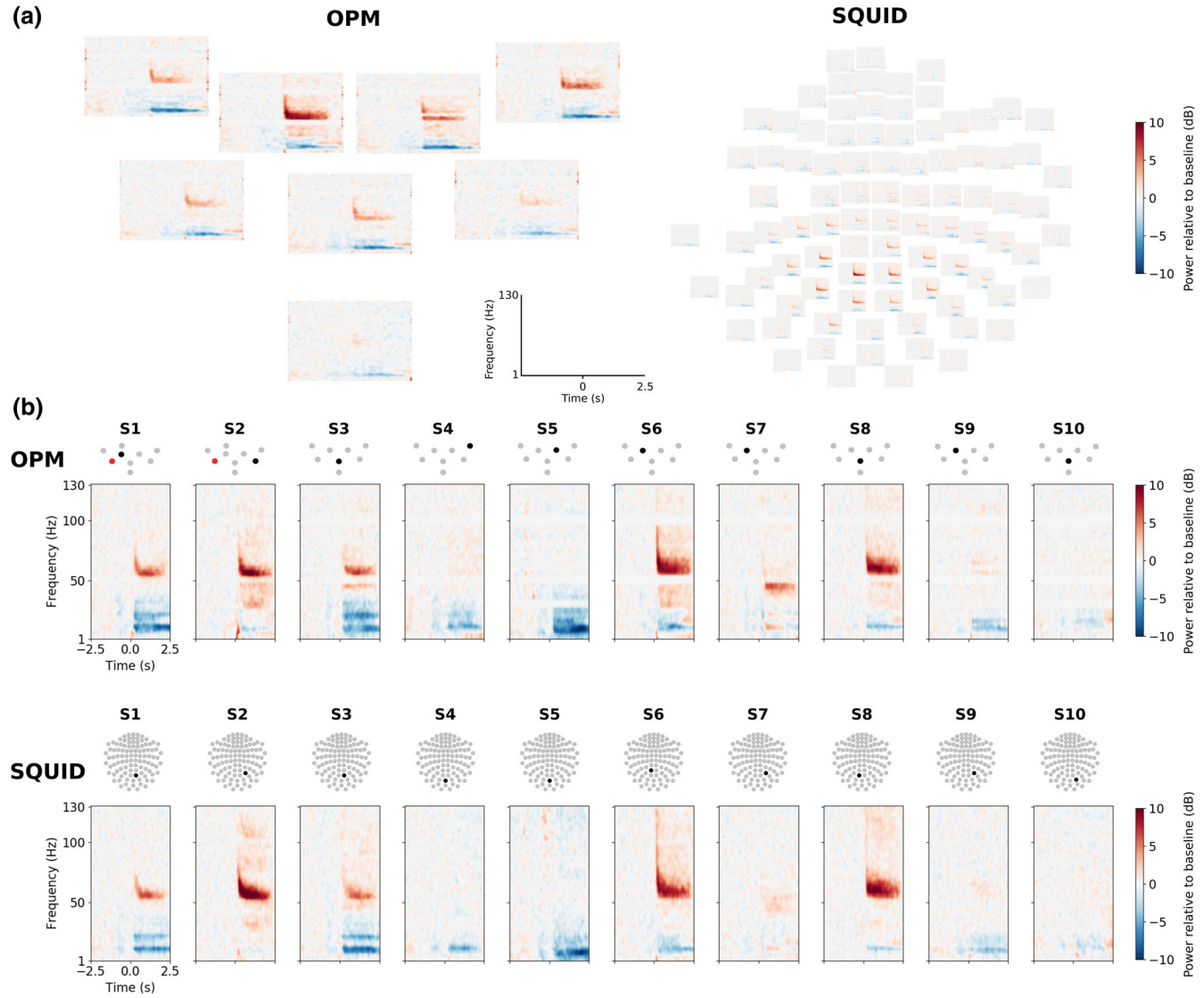

FIGURE 3 Time–frequency representations (TFRs) of the induced responses. (a) Responses in a representative subject (Subject 6) in optically pumped magnetometer (OPM; left) and SQUID (right) magnetometers. (b) TFRs of the sensors with the maximal-induced gamma-band response for OPMs (top row) and SQUID magnetometers (bottom row) across all subjects (one column per subject). The topographic sensor layouts indicate the sensor of the TFR (black) and a malfunctioning sensor (red) not included in the analysis

systematically larger than those for OPMs, we used the union of both bands to make the source estimates comparable between OPMs and SQUIDs. CSD computation was performed using a multitaper approach similar to that used for PSD estimation, with the bandwidth of the multitaper window function set to 1 Hz. Based on the CSD matrices, separate spatial filters were computed for, and applied to, each time period and frequency band to create time- and frequency-specific source-power estimates. Diagonal loading regularization of 0.01 was applied when computing the spatial filters. The source orientation which produced maximal power was chosen, and no weight normalization was applied. Finally, the baseline-normalized difference in source power ((Stimulation − Baseline)/Baseline) was computed for both frequency bands, and across-subject grand averages were computed after morphing the data to the "*fsaverage*" template brain (Fischl et al., 1999). The gamma-band grand-average was limited to those subjects for which clear gamma-band activity was present in the sensor-level analysis of both OPMs and SQUIDs, while all subjects were included for the alpha band grand-average. A comprehensive tutorial of this type of source analysis can be found in van Vliet, Liljeström, Aro, Salmelin, and Kujala (2018).

3 | RESULTS

3.1 | Sensor-level analysis

Examples of single-trial responses of all sensor types for Subject 6 are presented in Figure 2. Gamma-band (40–70 Hz) power increases are visible in these responses. Across the sensor types, the responses

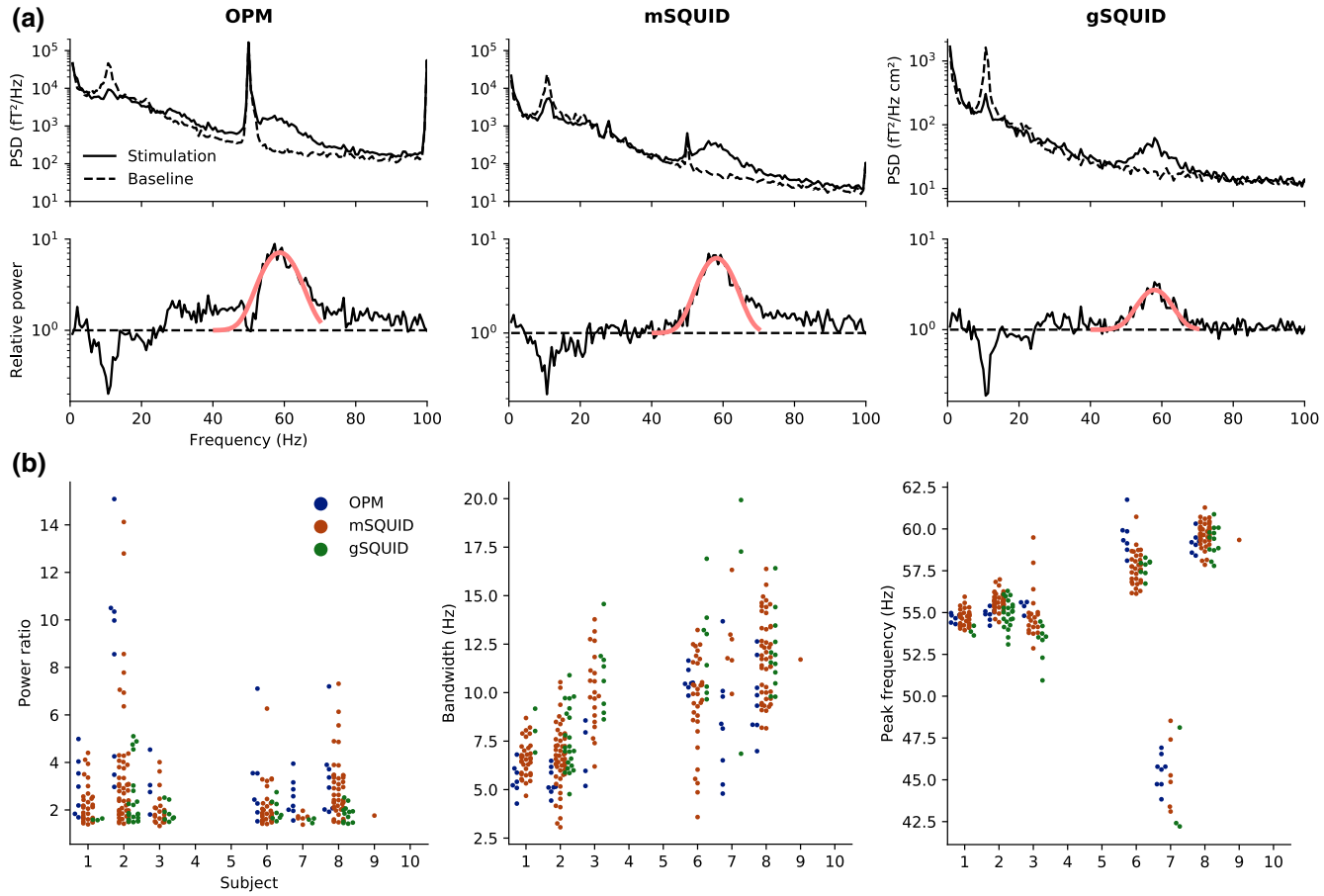

FIGURE 4 Power spectral analysis. (a) Top: Power spectral densities (PSDs) estimated prior and during stimulation for the sensor with the highest gamma-band power for optically pumped magnetometer (OPMs), SQUID magnetometers (mSQUID), and gradiometers (gSQUID) in a representative subject (Subject 6). Bottom: The ratio of the spectra (black) during stimulation and baseline, illustrating the power increase during stimulation, and the fitted Gaussian (red). (b) Relative power (stimulation vs. baseline), bandwidth, and peak frequency of the gamma response (extracted from the fitted Gaussian) across all subjects. The dots represent values for individual sensors

are qualitatively similar. The OPM signal amplitude is larger than that of SQUID magnetometer by roughly a factor of two.

Averaged TFR of the induced responses of OPM and SQUID magnetometers for Subject 6 are shown in Figure 3a. The TFR of the sensor with the maximum gamma-band response amplitude is presented in Figure 3b for each subject. Three out of the 10 subjects (Subjects 4, 5, and 10) did not show clear gamma-band activity for either OPM or SQUID measurements while they did show a decrease in alpha–beta power with both sensor types. Another four subjects (Subjects 2, 3, 6, and 8) demonstrated a simultaneous narrowband (40–70 Hz) and a possible broadband gamma increase.

The PSDs and the metrics derived from them are presented in Figure 4 for all subjects. Subject 9 shows gamma response only with one SQUID magnetometer. The goodness of the Gaussian fits to the PSDs of the sensors included in the analysis were 0.75 ± 0.13, 0.75 ± 0.13, and 0.68 ± 0.12 for OPMs, SQUID magnetometers and SQUID gradiometers, respectively (mean ± *SD*). For subjects with a considerable gamma-band response at any sensor, the number of sensors showing this response was 4–8, 1–50, and 3–22 for OPMs, SQUID magnetometers and gradiometers, respectively. Across the subjects and the sensors with a considerable gamma response, the average gamma power increase relative to baseline was 4.0, 2.7, and 2.1, while the maximum gamma power was 15.1, 14.1, and 5.1 for OPMs, SQUID magnetometers and gradiometers, respectively. The average subject-wise gamma power of the sensors with a considerable response ranged 2.5–8.1, 1.7–3.5, and 1.6–2.4 for OPMs, SQUID magnetometers, and gradiometers, respectively.

3.2 | Source-level analysis

Figure 5 shows the average source-power difference in alpha and gamma bands between stimulation and baseline for both OPMs and SQUID magnetometers. Gamma-band averages include subjects for which discernible gamma-band activity was present at the sensor level for both sensor types (Subjects 1, 2, 3, 6, 7, and 8); alpha-band averages include all subjects. For subject-level source estimates, see Figures S2 and S3, Supporting Information. The power difference in the grand-average source estimate was larger for OPMs than for SQUIDs in both

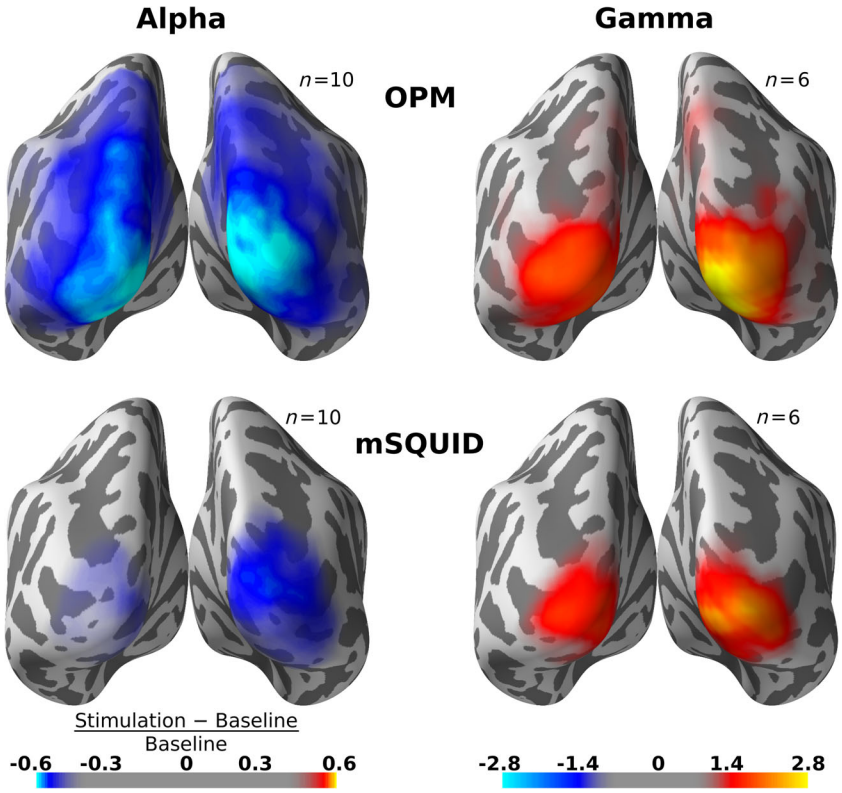

FIGURE 5 Grand-average normalized source-power difference between stimulation and baseline within alpha (7–13 Hz) and subject-specific gamma bands for optically pumped magnetometer (OPM; top row) and SQUID magnetometers (mSQUID, bottom row). The difference is visualized on the FreeSurfer "fsaverage" template brain. Color maps are the same for both sensor types

alpha and gamma bands. The laterality of the group-level gamma-power estimate is the same in OPMs and SQUIDs. The shape of the alpha-power estimate differs slightly between OPMs and SQUIDs.

4 | DISCUSSION

In this work, we applied an experimental paradigm known to elicit gamma-band activity in the early visual cortices while measuring both OPM-based on-scalp MEG and conventional SQUID-based MEG. We showed that this type of gamma activity is well visible in on-scalp OPM-MEG as well as in conventional MEG, with gamma SNR (as compared to the baseline power) typically being higher in on-scalp OPM-MEG. In particular, we showed that with an eight-channel OPM array group-level source estimates of alpha and gamma power are comparable to those obtained with a 102-channel SQUID magnetometer array.

4.1 | Gamma-band activity as measured by OPMs and SQUIDs

As Figures 3 and 4 demonstrate, gamma-band activity was seen with OPMs at least as well as with SQUID magnetometers. OPM signals have considerably higher absolute power than SQUIDs, as manifested already in the single-trial traces shown in Figure 2 and in the PSDs of Figure 4 due to the shorter distance between the OPMs and the neural sources.

Two subjects (2 and 6) displayed two separate bands in the gamma frequency range: one with a lower peak frequency around 30 Hz and another with a higher peak frequency (see TFRs of Figure 3 and PSDs of Figure 4a). Such a feature has also been observed earlier using the same stimuli (Hoogenboom et al., 2006). The lower gamma peak appeared more visible with OPMs than with SQUIDs in Subject 6 (see Figure 4a). It is unclear whether the lower frequency peak is due to broadband (>30 Hz) elevation of power giving an appearance of a separate peak, a subharmonic of the higher frequency gamma response, or an independent oscillation. However, it has been reported that in primate visual cortex multiple gamma peaks can be induced by large visual stimuli (Murty, Shirhatti, Ravishankar, & Ray, 2018).

In general, the gamma peak frequency varied considerably across subjects (Figures 3 and 4), which has also been reported in several earlier studies (Hoogenboom et al., 2006, 2010; van Pelt et al., 2018) and which seems to show some genetic dependence (van Pelt, Boomsma, & Fries, 2012) along with other factors such as sex and age (van Pelt et al., 2018). For some subjects, significant gamma-band activation was not detected in either OPM or SQUID measurements, at least not at the sensor level. Such a lack of visible gamma activity is also consistent with earlier literature, and may be due to many factors, such as differences in cortical folding, level of synchronous activity in cortical circuits, or even cognitive factors such as maintenance of the attentional focus on the stimulus.

The SQUID magnetometer and especially the OPM data exhibit significant 50-Hz line interference which could complicate detection and analysis of responses around 50 Hz. Fortunately, the gamma-band responses have relatively large bandwidth; the narrow 50-Hz interference peak only obscures a small portion of the gamma response. In the spectral analyses, the 50-Hz peak tends to decrease the values of the relative power at 50 Hz, as seen by the white lines

in the TFRs at 50 Hz (Figure 3) and the smaller power ratios around 50 Hz (Figure 4a). Using the Gaussian fits, we can estimate the shape of the underlying gamma response despite the interference peak; however, the peak can skew the fit to some degree, possibly explaining why the estimated gamma bandwidths are systematically smaller for OPMs than for SQUIDs.

The choice of baseline may affect the gamma power differences in Figure 4. For example, a slight alpha–beta suppression can be seen for some subjects during the baseline at approximately 1 s prior to stimulus onset (Figure 3). This MEG response corresponds to the dimming of the fixation dot, indicating that a trial will begin soon. Including this response to the baseline could change the obtained results. Indeed, the obtained power ratios changed slightly depending on which time windows were used for computing the baseline and stimulation spectra and what the lengths of those were; however, the relation between OPM, SQUID magnetometer, and SQUID gradiometer results remained unchanged. The inclusion of this time period in the baseline had no other visible effects on the results.

4.2 | Optimizing OPMs for detecting gamma-band activity

Due to the small number of sensors, the coverage of the cortex was limited in the OPM measurements. In addition, occipital areas were covered somewhat differently from subject to subject due to differences in the seating position and head shape; for some subjects, the OPM array was placed slightly too low to cover the whole occipital cortex adequately (see Figure S4, Supporting Information). When using partial-coverage arrays and similar positioning methods as described here, specific care must be taken when adjusting the relative positions of the sensors to the head in order to achieve good coverage of the region of interest.

Our OPM array consisted of eight sensors with an intersensor spacing of approximately 3.4 cm, which is far from the ideal; the spacing should be roughly the distance from the sensors to the brain (Ahonen et al., 1993), which is about 1.5 cm measured from the scalp. Thus, to maximize the amount of spatial detail present at the sensors and thus the spatial resolution of the method, an on-scalp array with sensor spacing less than 1.5 cm covering the region of interest in the brain would be optimal. In the case of the occipital cortex, this would correspond to ∼50 sensors.

The aforementioned limitations in sensor count and coverage and thus also in spatial sampling of the field limit our ability to fully utilize the benefits of on-scalp MEG arrays for modeling the neural sources. Nevertheless, we could successfully estimate the underlying sources from our OPM measurements, with the group-level estimates corresponding well to those based on the whole-head SQUID-magnetometer data (Figure 5). The subject-specific estimates also appear fairly similar for those subjects that had visible gamma-band activity at the sensor level (see Supporting Information).

In addition to sufficiently sampling the neuromagnetic field, MEG arrays should also reject external interference, for example, by using gradiometric techniques. SQUID-based MEG arrays typically comprise either gradiometers, magnetometers, or both gradiometers and magnetometers. Intrinsic OPM gradiometers can be constructed in several different ways, each with different advantages (see, e.g., Sheng, Perry, et al., 2017). In addition to noise rejection, gradiometers have implications for the spatial sampling of the neuromagnetic field (Ahonen et al., 1993). The optimal spatial sampling of an OPM array can be achieved not only by placing magnetometers densely, but also with sensor configurations using both magnetometers and gradiometers. OPM gradiometer parameters, such as baseline and type (axial vs. planar), remain to be optimized. Furthermore, by measuring more field components besides the field component normal to the scalp, the information content of the measurement can be increased (Iivanainen et al., 2017). Altogether, OPM array optimization is an interesting task for future research.

We have previously shown that the optical coregistration method we applied in the OPM measurement is sufficiently accurate for on-scalp MEG (Zetter et al., 2018, 2019). Thus, coregistration error should not be the limiting factor when improving OPM source estimates beyond those obtained from SQUID data. However, when OPM sensors are packed more densely, crosstalk between the sensors due to the sensor-wise modulation fields increases. With open-loop OPMs—such as the ones used here—crosstalk mainly changes the gain of the sensor and the orientation of its sensitive axis (Tierney et al., 2019). If crosstalk is not taken into account, it will cause source-estimation errors (Zetter et al., 2018). We do not believe that crosstalk will be a severe issue in dense open-loop OPM arrays. If the array geometry is fixed during the measurement, crosstalk will be constant and can, in principle, be taken into account by calibrating the sensor gains and sensitive axes. However, due to crosstalk, the sensing axes may not be normal to the scalp even if the sensors are physically placed as such. Additionally, with a careful design of sensor-wise coils, crosstalk can be minimized.

Due to the physics of the OPM sensors, their bandwidth is limited in comparison to SQUIDs, which have no intrinsic maximum measurable frequency as far as MEG measurements are concerned. The bandwidth of the OPMs employed in this work extends to ∼130 Hz (falling off 6 dB/octave), which is adequate for the narrowband gamma (40–70 Hz) we observed here. In contrast, invasively measured broadband gamma in the visual cortex has been shown to extend at least to 200 Hz (Hermes, Miller, Wandell, & Winawer, 2014). Thus, to study the entire gamma spectrum, the OPM bandwidth should be higher. In addition—besides broadband gamma—there are other high-frequency MEG signals beyond the current OPM bandwidth, for example, axonal ∼600-Hz -bursts (Curio, 2000) detected in S1 cortex in response to electric nerve stimulation as well as 150–250-Hz bursts linked to epileptic discharges (RamachandranNair et al., 2008; Zijlmans et al., 2012). As bandwidth and sensitivity are inherent trade-offs in OPMs (Budker & Romalis, 2007), further OPM sensor development is needed to meet the standards set by SQUIDs.

The current commercial OPMs can provide good-quality data, at least in environments where the ambient interference level is low, such as in our three-layer MSR. To increase the SNR of the gamma responses, the OPM noise level could be reduced: depending on the

subject, sensor noise (9–16 fT/$\sqrt{\text{Hz}}$ in our eight OPMs) in addition to the 1/*f* background brain activity (Buzsaki, 2006; Miller, Sorensen, Ojemann, & Den Nijs, 2009) was limiting the SNR of the gamma-band responses. From the spectrum of background brain activity as measured with OPMs, we estimate that to make the OPM measurement limited by the brain background activity within the OPM bandwidth (~130 Hz), the sensor noise level should be below 3 fT/$\sqrt{\text{Hz}}$.

Here, we used only eight OPMs to successfully record gamma-band activity. To study specific and localized brain activity with a good spatial resolution, such small arrays could be sufficient for many applications provided that the intersensor distance is short enough (<1.5 cm). These arrays could be operated in a typical shielded room augmented with active shielding against the static (Boto et al., 2018) or static and dynamic (Iivanainen et al., 2019) components of the ambient field. The sensor arrays could also be operated in a low-cost person-sized magnetic shield (e.g., Borna et al., 2017). Thus, we expect that MEG could be adopted more widely with the availability of OPMs and compact shields as one does not need an expensive whole-scalp MEG system in spacious surroundings for every MEG application.

4.3 | Narrowband versus broadband gamma

There seems to be two or more separate phenomena that are commonly referred to as gamma-band activity: synchronized, narrowband gamma oscillations as well as broadband gamma spanning at least 50–150 Hz (Lachaux et al., 2012). Narrowband gamma, which has also been termed "binding gamma" within the visual system, can be observed at least in the visual (e.g., Hoogenboom et al., 2006), somatomotor (e.g., Bauer, 2006; Gross, Schnitzler, Timmermann, & Ploner, 2007), and auditory systems (Brosch, Budinger, & Scheich, 2002). There are several hypotheses concerning its role (e.g., Donner & Siegel, 2011; Fries, 2015; Jensen & Mazaheri, 2010; Wang, 2010). Broadband gamma, on the other hand, is associated with a general increase in locally synchronous neuronal firing regardless of stimulus modality and brain region (Belitski et al., 2008; Liu & Newsome, 2006; Miller et al., 2014; Mukamel, 2005; Ray et al., 2008). Broadband gamma provides information about local processing in neuronal circuits and can thus serve as a highly focal marker of brain activity; for example, it can reveal spatial differences of the processing of highly similar stimuli (see, e.g., Flinker, Chang, Barbaro, Berger, & Knight, 2011). Whether and how narrowband and broadband gamma are related still remains an open question (Lachaux et al., 2012). Broadband gamma is often observed in invasive measurements (e.g., Bartoli et al., 2019; Cervenka et al., 2013; Crone et al., 2001; Crone, Sinai, & Korzeniewska, 2006; Edwards, Soltani, Deouell, Berger, & Knight, 2005; Hermes et al., 2014) but rarely in noninvasive ones.

In this work, we primarily studied narrowband gamma oscillations (here 40–70 Hz) to compare OPM and SQUID recordings. The narrowband visual gamma response to grating patterns seems to be well visible in MEG, as evidenced by the vast body of MEG studies using such stimuli to induce gamma-band activity in the visual cortex (e.g., Hoogenboom et al., 2006; Scheeringa et al., 2011; van Pelt et al., 2012, 2018). In contrast, we are not aware of any studies directly quantifying the broadband visual gamma response with MEG. One explanation why narrowband, but not broadband, gamma would be well visible in noninvasive recordings is that narrowband gamma may be spatially more coherent than broadband gamma. However, a recent study by Bartoli et al. (2019) showed that the sources of narrowband gamma responses to gratings are quite focal. They examined the narrowband gamma responses with high-density ECoG grids in the visual cortex and found that the grating stimulus elicited strong narrowband gamma response across electrodes; however, the phase correlation between the electrode responses decayed fast with an estimated spatial decay constant of 2.3–2.5 mm. The visibility of narrowband versus broadband gamma in noninvasive recordings is an intriguing question that calls for more research and explanations.

We briefly investigated higher frequency activity (>70 Hz), which should provide a proxy for broadband gamma, see Figure 3. Such high-frequency power increases were discernible in some of the TFRs and in the PSDs (see the tails of the PSDs in Figure 4). At the source level, a slight power increase within the 70–130-Hz band is seen during stimulation (especially with SQUIDs); see Figure S5, Supporting Information. A more extensive analysis and a larger data set with various visual stimuli would be needed for a more definitive comparison of broadband activity as measured by OPMs and SQUIDs.

As on-scalp MEG should have better spatial resolution than conventional SQUID-based MEG (Boto et al., 2016; Iivanainen et al., 2017), the use of on-scalp MEG to measure broadband gamma is attractive and could open a new noninvasive window into the functioning of the human brain. The noninvasive detection and localization of broadband gamma would be greatly facilitated by more sensitive OPM sensors assembled into arrays that provide dense spatial sampling of the neuromagnetic field and a good coverage of the cortical area of interest.

5 | CONCLUSIONS

We have shown that visual gamma-band responses can be measured with a small on-scalp OPM array with response quality comparable to that obtained with a conventional whole-scalp SQUID-based MEG. Gamma power and SNR were larger in OPMs compared to SQUIDs. To further facilitate the noninvasive detection of gamma-band activity, the on-scalp OPM arrays should be optimized with respect to sensor noise, the number of sensors, and intersensor spacing.

ACKNOWLEDGMENTS

Research reported here was supported by the European Research Council under ERC Grant Agreement no. 678578, the National Institute of Neurological Disorders and Stroke of the National Institutes of Health under Award Number R01NS094604, the Finnish Cultural Foundation under grant nos. 00170330 and 00180388 (J.I.) and the Instrumentarium Science Foundation under grant no. 180043 (R.Z.). The content is solely the responsibility of the authors and does not necessarily represent the official views of the funding organizations.

CONFLICT OF INTEREST

The authors declare no conflict of interest.

DATA AVAILABILITY STATEMENT

Data are not publicly available due to prohibition by Finnish law. As the consents given by the subjects only apply to the specific study reported in our manuscript, no portion of the human data collected can be used or released for use by third parties.

ORCID

Joonas Iivanainen https://orcid.org/0000-0001-6034-4604
Rasmus Zetter https://orcid.org/0000-0002-5331-2521
Lauri Parkkonen https://orcid.org/0000-0002-0130-0801

REFERENCES

Adjamian, P., Holliday, I. E., Barnes, G. R., Hillebrand, A., Hadjipapas, A., & Singh, K. D. (2004). Induced visual illusions and gamma oscillations in human primary visual cortex. *European Journal of Neuroscience*, *20*, 587–592. https://doi.org/10.1111/j.1460-9568.2004.03495.x

Ahonen, A. I., Hämäläinen, M. S., Ilmoniemi, R. J., Kajola, M. J., Knuutila, J. E., Simola, J. T., & Vilkman, V. A. (1993). Sampling theory for neuromagnetic detector arrays. *IEEE Transactions on Biomedical Engineering*, *40*, 859–869. https://doi.org/10.1109/10.245606

Ball, T., Demandt, E., Mutschler, I., Neitzel, E., Mehring, C., Vogt, K., … Schulze-Bonhage, A. (2008). Movement related activity in the high gamma range of the human EEG. *NeuroImage*, *41*, 302–310. https://doi.org/10.1016/j.neuroimage.2008.02.032

Bartoli, E., Bosking, W., Li, Y., Beauchamp, M. S., Yoshor, D., & Foster, B. (2019). Distinct narrow and broadband gamma responses in human visual cortex. *Cold Spring Harbor Laboratory*, bioRxiv. https://doi.org/10.1101/572313

Bauer, M. (2006). Tactile spatial attention enhances gamma-band activity in somatosensory cortex and reduces low-frequency activity in parieto-occipital areas. *Journal of Neuroscience*, *26*, 490–501. https://doi.org/10.1523/JNEUROSCI.5228-04.2006

Belitski, A., Gretton, A., Magri, C., Murayama, Y., Montemurro, M. A., Logothetis, N. K., & Panzeri, S. (2008). Low-frequency local field potentials and spikes in primary visual cortex convey independent visual information. *Journal of Neuroscience*, *28*, 5696–5709. https://doi.org/10.1523/JNEUROSCI.0009-08.2008

Borna, A., Carter, T. R., Goldberg, J. D., Colombo, A. P., Jau, Y.-Y., Berry, C., … Schwindt, P. D. (2017). A 20-channel magnetoencephalography system based on optically pumped magnetometers. *Physics in Medicine & Biology*, *62*, 8909–8923. https://doi.org/10.1088/1361-6560/aa93d1

Boto, E., Bowtell, R., Krüger, P., Fromhold, T. M., Morris, P. G., Meyer, S. S., … Brookes, M. J. (2016). On the potential of a new generation of magnetometers for MEG: A beamformer simulation study. *PLoS One*, *11*, e0157655. https://doi.org/10.1371/journal.pone.0157655

Boto, E., Holmes, N., Leggett, J., Roberts, G., Shah, V., Meyer, S. S., … Brookes, M. J. (2018). Moving magnetoencephalography towards real-world applications with a wearable system. *Nature*, *555*, 657–661. https://doi.org/10.1038/nature26147

Brosch, M., Budinger, E., & Scheich, H. (2002). Stimulus-related gamma oscillations in primate auditory cortex. *Journal of Neurophysiology*, *87*, 2715–2725. https://doi.org/10.1152/jn.2002.87.6.2715

Budker, D., & Kimball, D. F. J. (2013). *Optical magnetometry*. Cambridge: Cambridge University Press. https://doi.org/10.1017/CBO9780511846380

Budker, D., & Romalis, M. (2007). Optical magnetometry. *Nature Physics*, *3*, 227–234. https://doi.org/10.1038/nphys566

Buzsaki, G. (2006). *Rhythms of the brain*. New York, NY: Oxford University Press.

Cervenka, M. C., Franaszczuk, P. J., Crone, N. E., Hong, B., Caffo, B. S., Bhatt, P., … Boatman-Reich, D. (2013). Reliability of early cortical auditory gamma-band responses. *Clinical Neurophysiology*, *124*, 70–82. https://doi.org/10.1016/j.clinph.2012.06.003

Crone, N. (1998). Functional mapping of human sensorimotor cortex with electrocorticographic spectral analysis. II. Event-related synchronization in the gamma band. *Brain*, *121*, 2301–2315. https://doi.org/10.1093/brain/121.12.2301

Crone, N. E., Boatman, D., Gordon, B., & Hao, L. (2001). Induced electrocorticographic gamma activity during auditory perception. *Clinical Neurophysiology*, *112*, 565–582. https://doi.org/10.1016/S1388-2457(00)00545-9

Crone, N. E., Korzeniewska, A., & Franaszczuk, P. J. (2011). Cortical gamma responses: Searching high and low. *International Journal of Psychophysiology*, *79*, 9–15. https://doi.org/10.1016/j.ijpsycho.2010.10.013

Crone, N. E., Sinai, A., & Korzeniewska, A. (2006). High-frequency gamma oscillations and human brain mapping with electrocorticography. *Progress in Brain Research*, *159*, 275–295. https://doi.org/10.1016/S0079-6123(06)59019-3

Curio, G. (2000). Linking 600-Hz "Spikelike" EEG/MEG wavelets ("-bursts") to cellular substrates: Concepts and caveats. *Journal of Clinical Neurophysiology*, *17*, 377–396. https://doi.org/10.1097/00004691-200007000-00004

Dalal, S. S., Baillet, S., Adam, C., Ducorps, A., Schwartz, D., Jerbi, K., … Lachaux, J.-P. (2009). Simultaneous MEG and intracranial EEG recordings during attentive reading. *NeuroImage*, *45*, 1289–1304. https://doi.org/10.1016/j.neuroimage.2009.01.017

Dale, A. M., Fischl, B., & Sereno, M. I. (1999). Cortical surface-based analysis. I. Segmentation and surface reconstruction. *NeuroImage*, *9*, 179–194. https://doi.org/10.1006/nimg.1998.0395

Donner, T. H., & Siegel, M. (2011). A framework for local cortical oscillation patterns. *Trends in Cognitive Sciences*, *15*, 191–199. https://doi.org/10.1016/j.tics.2011.03.007

Eckhorn, R., Bauer, R., Jordan, W., Brosch, M., Kruse, W., Munk, M., & Reitboeck, H. J. (1988). Coherent oscillations: A mechanism of feature linking in the visual cortex? *Biological Cybernetics*, *60*, 121–130. https://doi.org/10.1007/BF00202899

Edwards, E., Soltani, M., Deouell, L. Y., Berger, M. S., & Knight, R. T. (2005). High gamma activity in response to deviant auditory stimuli recorded directly from human cortex. *Journal of Neurophysiology*, *94*, 4269–4280. https://doi.org/10.1152/jn.00324.2005

Fischl, B. (2012). FreeSurfer. *NeuroImage*, *62*, 774–781. https://doi.org/10.1016/j.neuroimage.2012.01.021

Fischl, B., Sereno, M. I., Tootell, R. B. H., & Dale, A. M. (1999). High-resolution intersubject averaging and a coordinate system for the cortical surface. *Human Brain Mapping*, *8*, 272–284. https://doi.org/10.1002/(SICI)1097-0193(1999)8:4<272::AID-HBM10>3.0.CO;2-4

Flinker, A., Chang, E. F., Barbaro, N. M., Berger, M. S., & Knight, R. T. (2011). Sub-centimeter language organization in the human temporal lobe. *Brain and Language*, *117*, 103–109. https://doi.org/10.1016/j.bandl.2010.09.009

Fries, P. (2015). Rhythms for cognition: Communication through coherence. *Neuron*, *88*, 220–235. https://doi.org/10.1016/j.neuron.2015.09.034

Fries, P., Reynolds, J. H., Rorie, A. E., & Desimone, R. (2001). Modulation of oscillatory neuronal synchronization by selective visual attention. *Science*, *291*, 1560–1563. https://doi.org/10.1126/science.1055465

Gramfort, A., Luessi, M., Larson, E., Engemann, D. A., Strohmeier, D., Brodbeck, C., … Hämäläinen, M. S. (2014). MNE software for processing MEG and EEG data. *NeuroImage*, *86*, 446–460. https://doi.org/10.1016/j.neuroimage.2013.10.027

Gray, C. M., König, P., Engel, A. K., & Singer, W. (1989). Oscillatory responses in cat visual cortex exhibit inter-columnar synchronization which reflects global stimulus properties. *Nature*, *338*, 334–337. https://doi.org/10.1038/338334a0

Gross, J., Kujala, J., Hämäläinen, M., Timmermann, L., Schnitzler, A., & Salmelin, R. (2001). Dynamic imaging of coherent sources: Studying neural interactions in the human brain. *Proceedings of the National Academy of Sciences of the United States of America*, *98*, 694–699. https://doi.org/10.1073/pnas.98.2.694

Gross, J., Schnitzler, A., Timmermann, L., & Ploner, M. (2007). Gamma oscillations in human primary somatosensory cortex reflect pain perception. *PLoS Biology*, *5*, e133. https://doi.org/10.1371/journal.pbio.0050133

Hämäläinen, M., Hari, R., Lounasmaa, O. V., Knuutila, J., & Ilmoniemi, R. J. (1993). Magnetoencephalography-theory, instrumentation, and applications to noninvasive studies of the working human brain. *Reviews of Modern Physics*, *65*, 413–497. https://doi.org/10.1103/RevModPhys.65.413

Hermes, D., Miller, K., Wandell, B., & Winawer, J. (2014). Stimulus dependence of gamma oscillations in human visual cortex. *Cerebral Cortex*, *25*, 2951–2959. https://doi.org/10.1093/cercor/bhu091

Hoogenboom, N., Schoffelen, J. M., Oostenveld, R., & Fries, P. (2010). Visually induced gamma-band activity predicts speed of change detection in humans. *NeuroImage*, *51*, 1162–1167. https://doi.org/10.1016/j.neuroimage.2010.03.041

Hoogenboom, N., Schoffelen, J. M., Oostenveld, R., Parkes, L. M., & Fries, P. (2006). Localizing human visual gamma-band activity in frequency, time and space. *NeuroImage*, *29*, 764–773. https://doi.org/10.1016/j.neuroimage.2005.08.043

Howard, M. W., Rizzuto, D. S., Caplan, J. B., Madsen, J. R., Lisman, J., Aschenbrenner-Scheibe, R., … Kahana, M. J. (2003). Gamma oscillations correlate with working memory load in humans. *Cerebral Cortex*, *13*, 1369–1374. https://doi.org/10.1093/cercor/bhg084

Iivanainen, J., Stenroos, M., & Parkkonen, L. (2017). Measuring MEG closer to the brain: Performance of on-scalp sensor arrays. *NeuroImage*, *147*, 542–553. https://doi.org/10.1016/j.neuroimage.2016.12.048

Iivanainen, J., Zetter, R., Grön, M., Hakkarainen, K., & Parkkonen, L. (2019). On-scalp MEG system utilizing an actively shielded array of optically-pumped magnetometers. *NeuroImage*, *194*, 244–258. https://doi.org/10.1016/j.neuroimage.2019.03.022

Jensen, O., & Mazaheri, A. (2010). Shaping functional architecture by oscillatory alpha activity: Gating by inhibition. *Frontiers in Human Neuroscience*, *4*, 186. https://doi.org/10.3389/fnhum.2010.00186

Jerbi, K., Ossandón, T., Hamamé, C. M., Senova, S., Dalal, S. S., Jung, J., … Lachaux, J. P. (2009). Task-related gamma-band dynamics from an intracerebral perspective: Review and implications for surface EEG and MEG. *Human Brain Mapping*, *30*, 1758–1771. https://doi.org/10.1002/hbm.20750

Jones, E., Oliphant, T., Peterson, P, and others. (2001). SciPy: Open source scientific tools for Python. http://www.scipy.org/.

Lachaux, J.-P., Axmacher, N., Mormann, F., Halgren, E., & Crone, N. E. (2012). High-frequency neural activity and human cognition: Past, present and possible future of intracranial EEG research. *Progress in Neurobiology*, *98*, 279–301. https://doi.org/10.1016/j.pneurobio.2012.06.008

Liu, J., & Newsome, W. T. (2006). Local field potential in cortical area MT: Stimulus tuning and behavioral correlations. *Journal of Neuroscience*, *26*, 7779–7790. https://doi.org/10.1523/JNEUROSCI.5052-05.2006

Manning, J. R., Jacobs, J., Fried, I., & Kahana, M. J. (2009). Broadband shifts in local field potential power spectra are correlated with single-neuron spiking in humans. *Journal of Neuroscience*, *29*, 13613–13620. https://doi.org/10.1523/JNEUROSCI.2041-09.2009

Miller, K. J., Honey, C. J., Hermes, D., Rao, R. P., denNijs, M., Ojemann, J. G. (2014). Broadband changes in the cortical surface potential track activation of functionally diverse neuronal populations. *NeuroImage*, *85*, 711–720. https://doi.org/10.1016/j.neuroimage.2013.08.070

Miller, K. J., Leuthardt, E. C., Schalk, G., Rao, R. P., Anderson, N. R., Moran, D. W., … Ojemann, J. G. (2007). Spectral changes in cortical surface potentials during motor movement. *Journal of Neuroscience*, *27*, 2424–2432. https://doi.org/10.1523/JNEUROSCI.3886-06.2007

Miller, K. J., Sorensen, L. B., Ojemann, J. G., & Den Nijs, M. (2009). Power-law scaling in the brain surface electric potential. *PLoS Computational Biology*, *5*, e1000609. https://doi.org/10.1371/journal.pcbi.1000609

Mukamel, R. (2005). Coupling between neuronal firing, field potentials, and fMRI in human auditory cortex. *Science*, *309*, 951–954. https://doi.org/10.1126/science.1110913

Murty, D. V., Shirhatti, V., Ravishankar, P., & Ray, S. (2018). Large visual stimuli induce two distinct gamma oscillations in primate visual cortex. *Journal of Neuroscience*, *38*, 2730–2744. https://doi.org/10.1523/JNEUROSCI.2270-17.2017

Pesaran, B., Pezaris, J. S., Sahani, M., Mitra, P. P., & Andersen, R. A. (2002). Temporal structure in neuronal activity during working memory in macaque parietal cortex. *Nature Neuroscience*, *5*, 805–811. https://doi.org/10.1038/nn890

Pfurtscheller, G., Graimann, B., Huggins, J. E., Levine, S. P., & Schuh, L. A. (2003). Spatiotemporal patterns of beta desynchronization and gamma synchronization in corticographic data during self-paced movement. *Clinical Neurophysiology*, *114*, 1226–1236. https://doi.org/10.1016/S1388-2457(03)00067-1

Pfurtscheller, G., & Neuper, C. (1992). Simultaneous EEG 10 Hz desynchronization and 40 Hz synchronization during finger movements. *Neuroreport*, *3*, 1057–1060. https://doi.org/10.1097/00001756-199212000-00006

RamachandranNair, R., Ochi, A., Imai, K., Benifla, M., Akiyama, T., Holowka, S., … Otsubo, H. (2008). Epileptic spasms in older pediatric patients: MEG and ictal high-frequency oscillations suggest focal-onset seizures in a subset of epileptic spasms. *Epilepsy Research*, *78*, 216–224. https://doi.org/10.1016/j.eplepsyres.2007.12.007

Ray, S., Crone, N. E., Niebur, E., Franaszczuk, P. J., & Hsiao, S. S. (2008). Neural correlates of high-gamma oscillations (60–200 Hz) in macaque local field potentials and their potential implications in electrocorticography. *Journal of Neuroscience*, *28*, 11526–11536. https://doi.org/10.1523/JNEUROSCI.2848-08.2008

Ray, S., & Maunsell, J. H. (2011). Different origins of gamma rhythm and high-gamma activity in macaque visual cortex. *PLoS Biology*, *9*, e1000610. https://doi.org/10.1371/journal.pbio.1000610

Scheeringa, R., Fries, P., Petersson, K.-M., Oostenveld, R., Grothe, I., Norris, D. G., … Bastiaansen, M. C. (2011). Neuronal dynamics underlying high-and low-frequency EEG oscillations contribute independently to the human BOLD signal. *Neuron*, *69*, 572–583. https://doi.org/10.1016/j.neuron.2010.11.044

Ségonne, F., Dale, A. M., Busa, E., Glessner, M., Salat, D., Hahn, H. K., & Fischl, B. (2004). A hybrid approach to the skull stripping problem in MRI. *NeuroImage*, *22*, 1060–1075. https://doi.org/10.1016/j.neuroimage.2004.03.032

Sheng, D., Perry, A. R., Krzyzewski, S. P., Geller, S., Kitching, J., & Knappe, S. (2017). A microfabricated optically-pumped magnetic gradiometer. *Applied Physics Letters*, *110*, 031106. https://doi.org/10.1063/1.4974349

Sheng, J., Wan, S., Sun, Y., Dou, R., Guo, Y., Wei, K., … Gao, J.-H. (2017). Magnetoencephalography with a Cs-based high-sensitivity compact atomic magnetometer. *Review of Scientific Instruments*, *88*, 094304. https://doi.org/10.1063/1.5001730

Singer, W. (1999). Neuronal synchrony: A versatile code for the definition of relations? *Neuron*, *24*, 49–65. https://doi.org/10.1016/S0896-6273(00)80821-1

Slepian, D. (1978). Prolate spheroidal wave functions, Fourier analysis, and uncertainty—V: The discrete case. *The Bell System Technical Journal*, *57*, 1371–1430. https://doi.org/10.1002/j.1538-7305.1978.tb02104.x

Srinivasan, R., Tucker, D. M., & Murias, M. (1998). Estimating the spatial Nyquist of the human EEG. *Behavior Research Methods, Instruments, & Computers*, *30*, 8–19. https://doi.org/10.3758/BF03209412

Stenroos, M., & Nummenmaa, A. (2016). Incorporating and compensating cerebrospinal fluid in surface-based forward models of magneto- and electroencephalography. *PLoS One*, *11*, 1–23. https://doi.org/10.1371/journal.pone.0159595

Tallon-Baudry, C., Bertrand, O., Delpuech, C., & Pernier, J. (1996). Stimulus specificity of phase-locked and non-phase-locked 40 Hz visual responses in human. *The Journal of Neuroscience: The Official Journal of the Society for Neuroscience*, *16*, 4240–4249. https://doi.org/10.1016/j.neuropsychologia.2011.02.038

Tan, H.-R., Gross, J., & Uhlhaas, P. (2016). MEG sensor and source measures of visually induced gamma-band oscillations are highly reliable. *NeuroImage*, *137*, 34–44. https://doi.org/10.1016/j.neuroimage.2016.05.006

Tierney, T. M., Holmes, N., Mellor, S., López, J. D., Roberts, G., Hill, R. M., … Barnes, G. R. (2019). Optically pumped magnetometers: From quantum origins to multi-channel magnetoencephalography. *NeuroImage*, *199*, 598–608. https://doi.org/10.1016/j.neuroimage.2019.05.063

Uusitalo, M. A., & Ilmoniemi, R. J. (1997). Signal-space projection method for separating MEG or EEG into components. *Medical and Biological Engineering and Computing*, *35*, 135–140. https://doi.org/10.1007/BF02534144

van Pelt, S., Boomsma, D. I., & Fries, P. (2012). Magnetoencephalography in twins reveals a strong genetic determination of the peak frequency of visually induced gamma-band synchronization. *Journal of Neuroscience*, *32*, 3388–3392. https://doi.org/10.1523/JNEUROSCI.5592-11.2012

van Pelt, S., Shumskaya, E., & Fries, P. (2018). Cortical volume and sex influence visual gamma. *NeuroImage*, *178*, 702–712. https://doi.org/10.1016/j.neuroimage.2018.06.005

van Vliet, M., Liljeström, M., Aro, S., Salmelin, R., & Kujala, J. (2018). Analysis of functional connectivity and oscillatory power using DICS: From raw MEG data to group-level statistics in python. *Frontiers in Neuroscience*, *12*, 586. https://doi.org/10.3389/fnins.2018.00586

Wang, X.-J. (2010). Neurophysiological and computational principles of cortical rhythms in cognition. *Physiological Reviews*, *90*, 1195–1268. https://doi.org/10.1152/physrev.00035.2008

Zetter, R., Iivanainen, J., & Parkkonen, L. (2019). Optical co-registration of MRI and on-scalp MEG. *Scientific Reports*, *9*, 5490. https://doi.org/10.1038/s41598-019-41763-4

Zetter, R., Iivanainen, J., Stenroos, M., & Parkkonen, L. (2018). Requirements for coregistration accuracy in on-scalp MEG. *Brain Topography*, *31*, 931–948. https://doi.org/10.1007/s10548-018-0656-5

Zijlmans, M., Jiruska, P., Zelmann, R., Leijten, F. S., Jefferys, J. G., & Gotman, J. (2012). High-frequency oscillations as a new biomarker in epilepsy. *Annals of Neurology*, *71*, 169–178. https://doi.org/10.1002/ana.22548

SUPPORTING INFORMATION

Additional supporting information may be found online in the Supporting Information section at the end of this article.

How to cite this article: Iivanainen J, Zetter R, Parkkonen L. Potential of on-scalp MEG: Robust detection of human visual gamma-band responses. *Hum Brain Mapp*. 2020;41:150–161. https://doi.org/10.1002/hbm.24795